nature nanotechnology

Article

https://doi.org/10.1038/s41565-025-02029-5

Magnetically tunable selectivity in methane oxidation enabled by Fe-embedded liquid metal catalysts

Received: 11 December 2022

Accepted: 4 September 2025

Published online: 3 November 2025

Check for updates

Haoran Zhang[1,2,9], Yinhe Wang[2,9], Yu Zhang[1,2,9], Fan Wu[2], Rui Huang[1], Sicong Wang[3], Xiaokang Liu[3], Yihua Ran[4,5], Zhiwen Zhang[1], Jun Cai[4,5], Huang Zhou[1], Tao Yao[3], Jun Jiang[2], Zhi Liu[4,5], Yu Mao[6], Wenhui Zhong[7] ✉, Lin Hu[8] ✉, Lei Zheng[6] ✉ & Yuen Wu[1,2] ✉

As they are liquids at room temperature, gallium-based metal substrates allow catalytic metal atoms to move freely without lattice constraints, thereby facilitating the development of catalysts with reconfigurable structures. Here we design an iron-embedded liquid metal catalyst that enables reversible switching of the aggregation and electron spin of iron atoms by controlling an external magnetic field. This facilitates a reversible conversion of the primary liquid products, methyl hydroperoxide (CH_3OOH) and acetic acid (CH_3COOH), under ambient conditions. The catalyst achieves promising production rates (CH_3OOH, 1,679.6 mmol g_{Fe}^{-1} h^{-1}; CH_3COOH, 790.5 mmol g_{Fe}^{-1} h^{-1}) and high selectivities (CH_3OOH, 99.9%; CH_3COOH, 91.7%). In the absence of the magnetic field, iron atoms are atomically dispersed, leading to the C1 pathway without C–C bond coupling. When a magnetic field is applied, iron atoms cluster, favouring CH_3COOH production in the C2 pathway. The product distribution can be finely and reversibly tuned with magnetic field intensity adjustments ranging from 0 to 500 G. Our findings highlight the potential for using an external magnetic field to precisely control catalytic pathways.

Traditional CH_4 oxidation catalysts are primarily based on solid materials in which the chemical environment of the active sites determines the catalyst's activity and selectivity. Single-atom catalysts, due to their unique singular active sites, typically yield only C1 products, whereas clusters or particles with multiple atomic sites commonly produce C2 or longer-chain hydrocarbons[1–5]. However, these solid catalysts have an inherent flaw: their rigid solid structure restricts the ability to modify the chemical configuration of active sites during reactions. This notably limits the possibility of adjusting catalytic activity and selectivity during the reaction process.

Liquid metals, as emerging materials, present a novel approach for developing CH_4 oxidation catalysts. Their unique physical and chemical properties, such as low melting point, high thermal conductivity and excellent chemical stability, make them ideal catalyst carriers[6,7], capable of dissolving specific metals and achieving stable dispersion at the atomic level[8]. In contrast to solid catalysts, liquid metals remain

[1]State Key Laboratory of Precision and Intelligent Chemistry/School of Chemistry and Materials Science, University of Science and Technology of China, Hefei, China. [2]Deep Space Exploration Laboratory, University of Science and Technology of China, Hefei, China. [3]National Synchrotron Radiation Laboratory, University of Science and Technology of China, Hefei, China. [4]School of Physical Science and Technology, Shanghai Tech University, Shanghai, China. [5]State Key Laboratory of Functional Materials for Informatics, Shanghai Institute of Microsystem and Information Technology, Chinese Academy of Sciences, Shanghai, China. [6]School of Food and Biological Engineering, Hefei University of Technology, Hefei, China. [7]Institute of Intelligent Innovation, Henan Academy of Sciences, Zhengzhou, China. [8]Anhui Province Key Laboratory of Condensed Matter Physics at Extreme Conditions, High Magnetic Field Laboratory, Chinese Academy of Sciences, Hefei, China. [9]These authors contributed equally: Haoran Zhang, Yinhe Wang, Yu Zhang. ✉e-mail: whzhong@hnas.ac.cn; hulin@hmfl.ac.cn; lzheng@hfut.edu.cn; yuenwu@ustc.edu.cn

https://doi.org/10.1038/s41565-025-02029-5

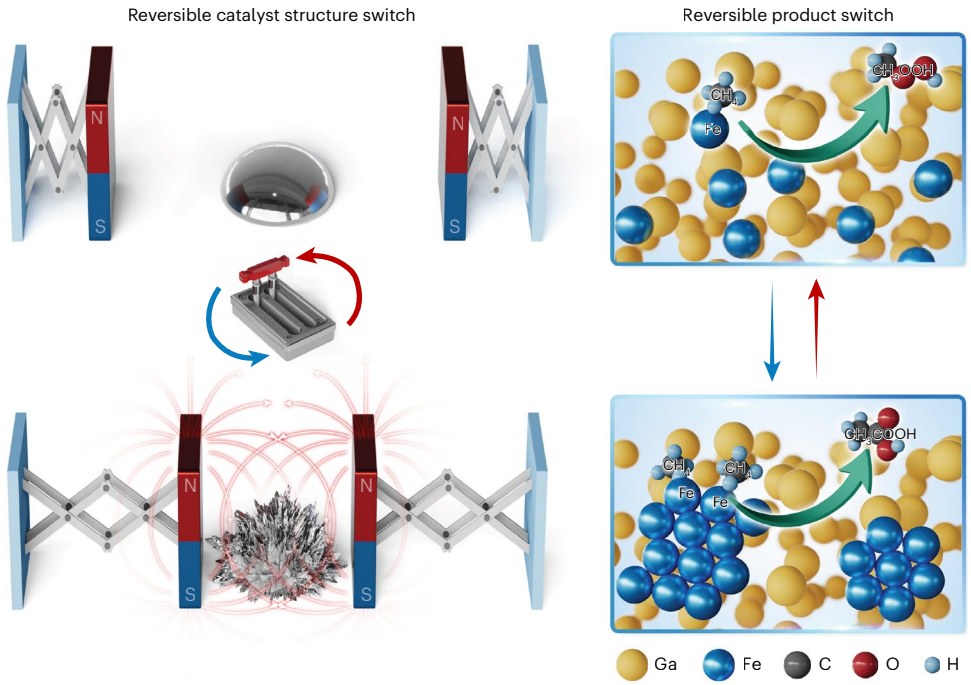

Fig. 1 | Schematic of the mechanism. Schematic diagram of macroscopic (left) and microstructural (right) changes in Fe–LMS under the control of a magnetic field switch.

liquid at room temperature, with atoms not confined by a lattice, thus offering the possibility of dynamically adjustable structures. Unlike traditional catalytic adjustment methods, including the application of thermal, optical and electric fields, a magnetic field is easily generated by permanent magnets, and allows for external control of catalytic reactions under milder conditions. Recent studies on magnet-assisted catalysis have primarily focused on manipulating the electron spins at the catalytic centre to improve the adsorption and mass transfer of reactive molecules[9–11].

Here we show a magnetic-field-responsive catalyst composed of an iron-embedded, catalytically active liquid metal solution (Fe–LMS), and a eutectic alloy, galinstan, as a weak-binding substrate. This Fe–LMS catalyst responds to changes in external magnetic field intensity, enabling a reversible and rapid rearrangement of iron atoms between isolated single atoms (Fe_1–LMS) and agglomerated clusters (Fe_n–LMS) (Fig. 1, left). As a result, we achieve reversible conversion of the main liquid product of CH_4 oxidation between CH_3OOH and CH_3COOH with high production rates (1,679.6 mmol g_{Fe}^{-1} h^{-1} and 790.5 mmol g_{Fe}^{-1} h^{-1}, respectively) and high selectivities (99.9% and 91.7%, respectively) under a field of 0–500 G at room temperature (Fig. 1, right). Through in situ measurements and theoretical calculations, we find that the magnetic field switching influences the nanostructure, local coordination environment and electron spin of Fe–LMS, leading to the generation of intermediate species that determine the reaction pathways of C1 or C2. In particular, the change in the aggregation state and spin state of iron atoms in the presence of the external magnetic field breaks the adsorption energy scaling relationship with reactive molecules, altering reaction selectivity.

Characterization of the catalyst with a sensitive magnetic field response

In this work, Fe–LMS catalyst supported on liquid galinstan alloy was used for the selective oxidation of CH_4. Supplementary Fig. 1 and Supplementary Movie 1 provide a macroscopic perspective of the reversible morphological changes in a Fe–LMS droplet under the influence of a magnetic field. The transmission electron microscopy (TEM), scanning electron microscopy (SEM) and aberration-corrected scanning transmission electron microscopy (STEM) images in Supplementary Fig. 2 and Fig. 2a reveal that ultrasonically dispersed Fe–LMS microdroplets present a perfect sphere with a smooth edge. The energy-dispersive X-ray spectroscopy (EDS) image in Fig. 2b confirms the uniform distribution of gallium, indium and tin in galinstan, and an iron loading of around 1% (Supplementary Table 1) is observed to be evenly spread over the Fe–LMS microdroplet. In situ X-ray two-dimensional computed tomography (2D CT) slice (Fig. 2c) and 3D views (Supplementary Fig. 3) reveal a uniform, symmetric spherical distribution of iron under 0 G. The 2D CT slice (Fig. 2d) and 3D views (Supplementary Fig. 3) show a notable deviation under 500 G, with iron atoms aggregating towards one side, indicating the influence of the field on their spatial arrangement.

We used atomic-level-resolution high-angle annular dark-field scanning transmission electron microscopy (HAADF-STEM) and corresponding high-resolution energy-dispersive X-ray spectroscopy (EDS) mapping. Without a magnetic field, the sample shows amorphous dispersion of iron/gallium atoms (Fig. 2e–h). In contrast, a 500-G magnetic field induces α-Fe(100) cluster formation (0.206-nm lattice spacing, Fig. 2i–l), while gallium remains uniformly distributed. Quantitative EDS confirms magnetic-field-driven iron aggregation without altering the gallium distribution (Supplementary Fig. 4).

X-ray absorption fine structure (XAFS) analysis reveals magnetic-field-induced structural reorganization in Fe–LMS. At 1 wt% iron loading and zero-field conditions, the R-space spectra shows a single coordination peak, while 500-G exposure generates additional peaks at 3.7 Å and 4.5 Å (second and third nearest-neighbour coordination, Fig. 2m), similar to those seen in iron foil and indicating reversible iron aggregation (Supplementary Fig. 5). Higher iron loading (10 wt%) inherently exhibits these features (Supplementary Fig. 6). X-ray absorption near-edge spectra (Supplementary Fig. 7) and k-space data (Supplementary Fig. 8) further confirm distinct coordination environments between dispersed and aggregated state samples. Curve fitting (Supplementary Figs. 9–11 and Supplementary Table 2) demonstrates gallium as the primary coordination shell for iron in 1 wt% Fe–LMS, with Fe–Fe bonds emerging via magnetic-field application. Self-absorption effects were systematically excluded through fluorescence-mode XAFS

https://doi.org/10.1038/s41565-025-02029-5

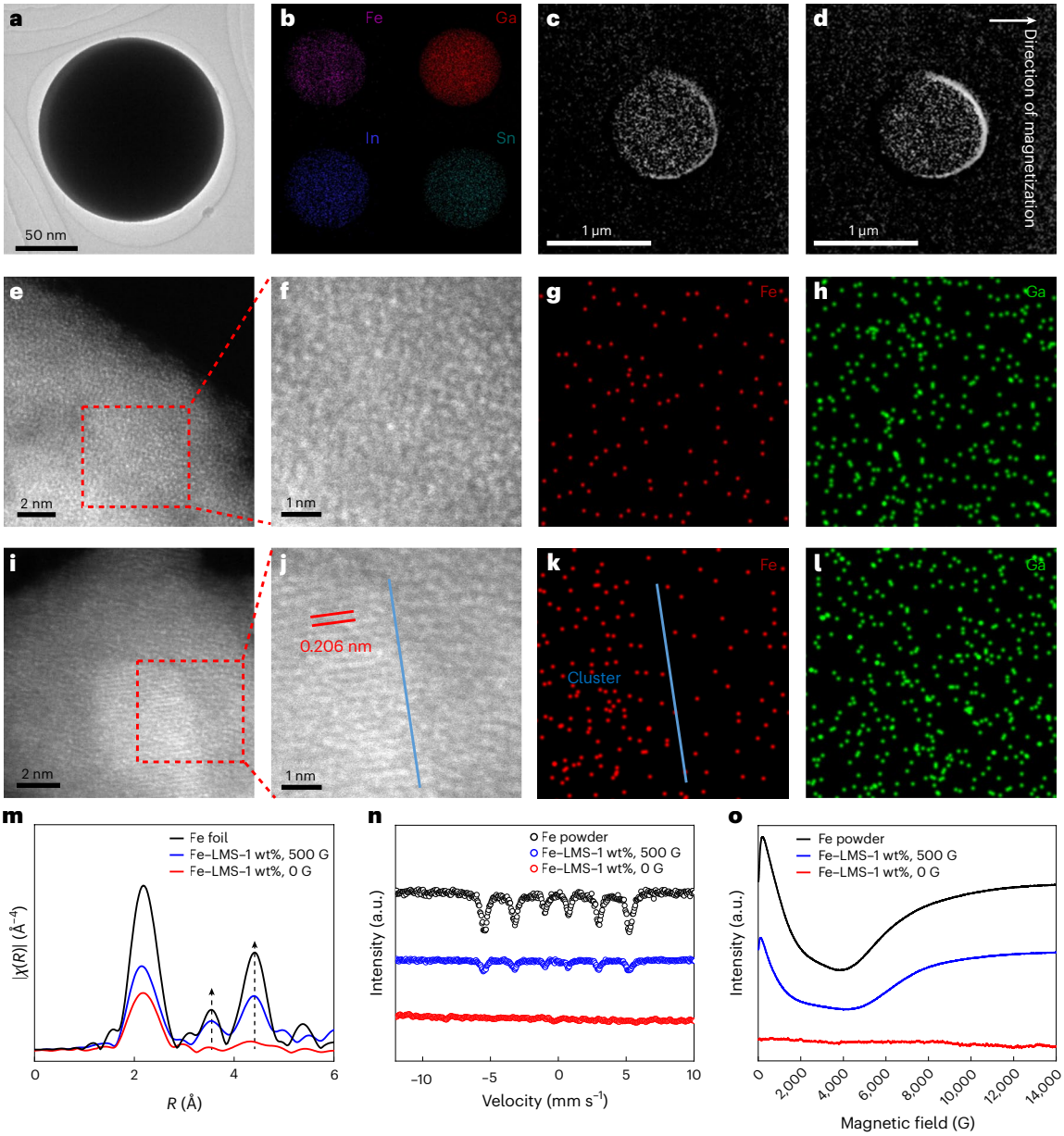

Fig. 2 | Characterization of Fe–LMS. a,**b**, STEM (**a**) and EDS elemental mapping (**b**) images of Fe–LMS. **c**, 2D CT reconstruction images for Fe–LMS under 0 G. **d**, 2D CT reconstruction images for Fe–LMS under 500 G. **e**, HAADF-STEM images for Fe–LMS under 0 G. **f**, Partially enlarged image of **e**. **g**, The corresponding iron EDS mappings for **f**. **h**, The corresponding gallium EDS mappings for **f**. **i**, HAADF-STEM images for Fe–LMS under 500 G. **j**, Partially enlarged image of **i**. **k**, The corresponding iron EDS mappings for **j**. **l**, The corresponding gallium EDS mappings for **j**. **m**, Iron K-edge EXAFS spectra in *R* space for the iron foil, Fe–LMS–1 wt% (0 G) and Fe–LMS–1 wt% (0 G). **n**, Mössbauer spectra for iron standard sample under 0 G, Fe–LMS–1 wt% under 0 G and Fe–LMS–1 wt% under 500 G. **o**, ESR absorption versus magnetic field for iron standard sample, Fe–LMS–1 wt% under 0 G and Fe–LMS–1 wt% under 500 G.

measurements at a range of incident angles (Supplementary Fig. 12), validating data reliability.

In situ Mössbauer spectroscopy was used to characterize the catalyst's structure. Due to the measurement principle, free atoms are excited to emit photons, experiencing recoil momentum and preventing resonance absorption detection, whereas lattice-embedded clusters show negligible recoil, enabling measurable signals[12–15]. Under zero-field conditions, the absence of detectable signals (Fig. 2n) confirms atomically dispersed iron. Under 500 G, a signal peak with a shape remarkably similar to that of the iron reference sample is observed (see fitting data in Supplementary Fig. 13 and Supplementary Table 3), demonstrating magnetic-field-driven cluster formation. Electron spin resonance (ESR) measurements further corroborate this transition, showing standard-like ferromagnetic signatures only under magnetic fields, while zero-field conditions exhibit weak signals due to gallium-mediated spin relaxation (Fig. 2o)[16–18]. The system shows near-instantaneous magnetic response (Supplementary Fig. 14), with magnetization scaling linearly with field intensity and complete reversibility upon field removal.

Switching of methane oxidation reaction pathway regulated by magnetic field

The CH_4 oxidation reaction was conducted in a high-pressure autoclave (2 MPa CH_4) using Fe–LMS droplet catalysts and diluted H_2O_2. The reactor was placed between adjustable magnets (0–500 G). Products were analysed by gas chromatography (GC) and ^{1}H NMR. Gallium-based substrates required indium/tin additives to reduce melting points (see phase diagrams in Supplementary Fig. 16). Ga–In and Ga–Sn exhibited

https://doi.org/10.1038/s41565-025-02029-5

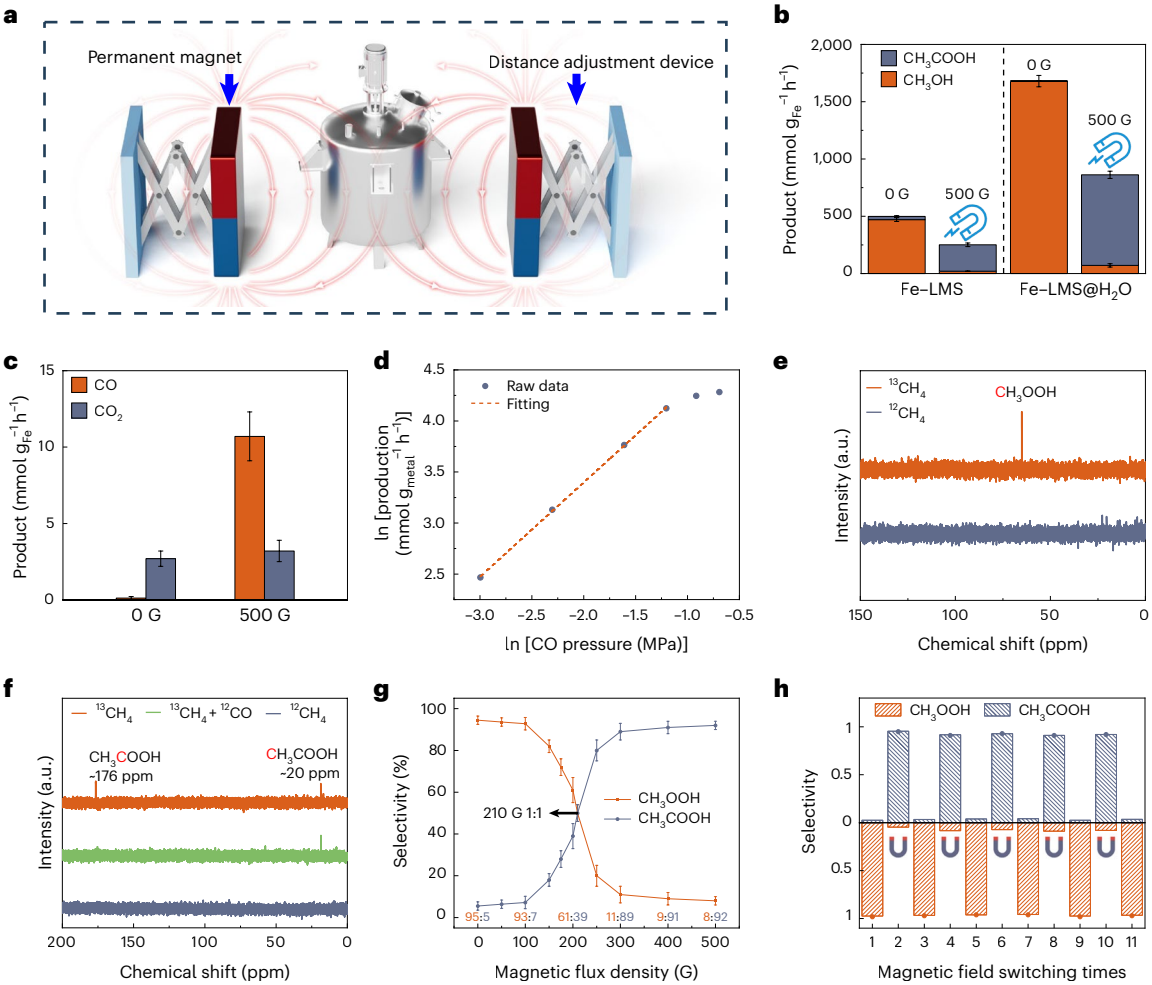

Fig. 3 | Catalytic performance in CH_4 oxidation. a, Schematic diagram of the reaction device. **b**, Production rates of liquid products (CH_3OOH and CH_3COOH) for Fe–LMS controlled by an external magnetic field. Data are represented as the mean ± s.d. from five parallel experiments. **c**, Production rates of gaseous products (CO and CO_2) for Fe–LMS controlled by an external magnetic field. Data are represented as the mean ± s.d. from five parallel experiments. **d**, Correlation between the production rate of CH_3COOH and additionally applied CO partial pressure for Fe–LMS@H_2O under a 500-G magnetic field. **e**, ^{13}C NMR spectra of liquid product for Fe–LMS without a magnetic field. Experimental conditions: 2 MPa $^{13}CH_4$, 25 ml H_2O_2 (6%), pH 4, r.t., 1 h (red line); 2 MPa $^{12}CH_4$, 25 ml H_2O_2 (6%), pH 4, r.t., 1 h (grey line). **f**, ^{13}C NMR spectra of liquid product for Fe–LMS with a 500-G magnetic field. Experimental conditions: 2 MPa $^{13}CH_4$, 25 ml H_2O_2 (6%), pH 4, r.t., 1 h (red line); 2 MPa $^{13}CH_4$ + 0.5 MPa ^{12}CO, 25 ml H_2O_2 (6%), pH 4, r.t., 1 h (green line); 2 MPa $^{12}CH_4$, 25 ml H_2O_2 (6%), pH 4, r.t., 1 h (grey line). **g**, Correlation between selectivity of liquid products and magnetic induction intensity. Data are represented as the mean ± s.d. from five parallel experiments. **h**, Selectivity of CH_3COOH for Fe–LMS when applying multiple off–on operations of a magnetic field. Each operation lasts for 1 h and CH_4 is refilled after each operation.

catalytic activity comparable to that of galinstan, confirming their primary role as melting-point depressants (Supplementary Fig. 17). Given that the galinstan alloy formulation demonstrates the most notable melting point depression and is widely used in applications[19–21], it was selected as the liquid metal substrate in this work. The Fe–LMS-catalysed CH_4 oxidation reaction generates two main kinds of liquid (CH_3OOH and CH_3COOH) and gas (CO and CO_2) products (Fig. 3b,c and Supplementary Figs. 18 and 19), respectively.

Given H_2O_2's strong oxidative nature, potential metal oxide formation from Fe–LMS was evaluated. Catalytic testing (Supplementary Fig. 20) confirmed negligible contributions of all possible metal oxides to liquid product yields, irrespective of magnetic field application. Supplementary Fig. 21 reveals that mild acidity (pH ≈ 4) achieves relatively high yields of both CH_3OOH and CH_3COOH, whereas extreme pH values degrade catalytic activity. This pH condition was selected as optimal for dual-product generation under magnetic field modulation and adopted as the standard for subsequent experiments. Supplementary Fig. 22 confirms negligible Cl^- influence from HCl using NaCl concentration gradients. Optimal activity occurs with 6% H_2O_2 (Supplementary Fig. 23), demonstrating the necessity of HCl/H_2O_2 synergy to maintain surface oxidation states. Visual evidence (Supplementary Fig. 24) shows that Fe–LMS retains spherical morphology only at pH 4 with 6% H_2O_2, while other conditions (pH 7 or 15% H_2O_2) induce oxidation.

Without magnetic fields, Fe–LMS primarily produces CH_3OOH (471.1 mmol g_{Fe}^{-1} h^{-1}, 94.5%). Under 500 G, product selectivity reverses, yielding CH_3COOH as the main product (230.6 mmol g_{Fe}^{-1} h^{-1}, 91.9%). Production rates scale linearly with iron loading (Supplementary Fig. 25), while long-term tests (48 h, Supplementary Fig. 26) show stable C1 yields (zero-field) or steady CH_3COOH production (~90% selectivity, magnetic field). Ultrasonic dispersion yields 100-nm Fe–LMS@H_2O droplets (Supplementary Fig. 27), maintaining size postreaction. This enhances catalytic surface area, tripling both CH_3OOH (1,679.6 mmol g_{Fe}^{-1} h^{-1}, 99.9%) and CH_3COOH (790.5 mmol g_{Fe}^{-1} h^{-1}, 91.7%) production rates (Fig. 3b). Such high generation rates of CH_3OOH and CH_3COOH both attain excellent levels in the thermocatalytic field of CH_4 oxidation as displayed in Supplementary Table 4.

Under 500 G, CO production increases sharply whereas CO_2 yield remains stable (Fig. 3c). Previous studies reported that mixing CO into CH_4 as a coreactant leads to the formation of CH_3COOH[22,23].

https://doi.org/10.1038/s41565-025-02029-5

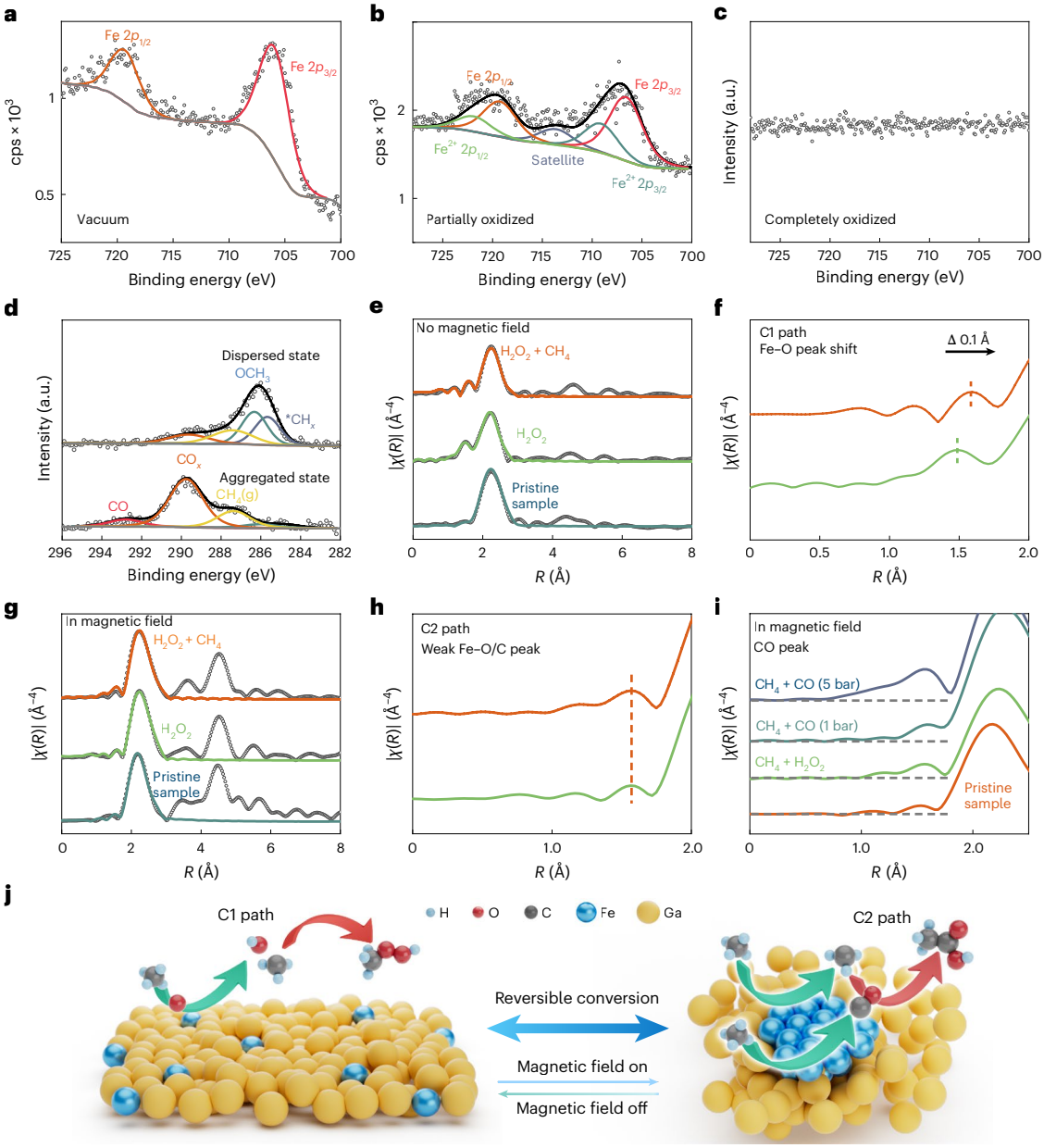

Fig. 4 | In situ experiments and mechanism exploration. a, NAP-XPS spectra for Fe–LMS (1 wt% iron loading) in a vacuum environment. cps, counts per second. **b**, NAP-XPS spectra for Fe–LMS (1 wt% iron loading) in a 0.13-mbar H_2O_2 solution (30%) vapour atmosphere. **c**, NAP-XPS spectra for Fe–LMS (1 wt% iron loading) following a 24-h exposure to a 0.13-mbar H_2O_2 (30%) vapour atmosphere. **d**, NAP-XPS spectra for dispersed-state and aggregated-state catalysts. **e**, Iron K-edge EXAFS spectra in *R* space recorded without a magnetic field for pristine Fe–LMS, Fe–LMS immersed in H_2O_2, and Fe–LMS under reaction conditions. **f**, Partially enlarged image of **c** (dashed line indicates the peak position). **g**, Iron K-edge EXAFS spectra in *R* space recorded under a 500-G magnetic field for pristine Fe–LMS, Fe–LMS–B immersed in H_2O_2, and Fe–LMS–B under reaction conditions. **h**, Partially enlarged image of **d** (dashed line indicates the peak position). **i**, Iron K-edge EXAFS spectra in *R* space recorded under a 500-G magnetic field for Fe–LMS–B with H_2O_2, Fe–LMS–B under reaction conditions, and Fe–LMS–B with an additional 1 bar and 5 bar CO beyond the reaction conditions. **j**, Schematic diagram of reversible regulation of structure changes by magnetic field switches leading to changes in reaction pathways.

There is a linear increase in CH_3COOH yield with higher CO/CH_4 ratios under magnetic fields (Fig. 3d). In the absence of a magnetic field, the introduction of CO only slightly increased the yield of CH_3COOH (Supplementary Fig. 28), with the main product on the dispersed-state Fe–LMS remaining CH_3OOH. ^{13}C NMR analysis confirmed distinct carbon sources for CH_3OOH and CH_3COOH (Fig. 3e,f). CH_3OOH was derived exclusively from $^{13}CH_4$, while CH_3COOH showed characteristic peaks at 176 ppm (carbonyl) and 20 ppm (methyl)[24]. Introducing ^{12}CO into $^{13}CH_4$ (4:1) reduced the carbonyl signal, demonstrating CO's role as a key intermediate in CH_3COOH formation. Product selectivity is magnetically tunable, with CH_3OOH:CH_3COOH ratios shifting progressively from 95:5 (0 G) to 8:92 (500 G) (Fig. 3g). The system exhibits robust reversibility, maintaining CH_3OOH (>90%) and CH_3COOH (> 80%) selectivity over 11 magnetic switching cycles (Fig. 3h), demonstrating precise control over product distribution via field intensity.

In situ experiment and mechanism exploration

Ambient-pressure X-ray photoelectron spectroscopy (APXPS) was performed to investigate the real chemical environment during the reaction process (Supplementary Fig. 29). In a vacuum environment, an Fe(0) signal was detected (Fig. 4a). Upon the introduction of oxidants, the iron signal intensified, and the oxidation state increased

https://doi.org/10.1038/s41565-025-02029-5

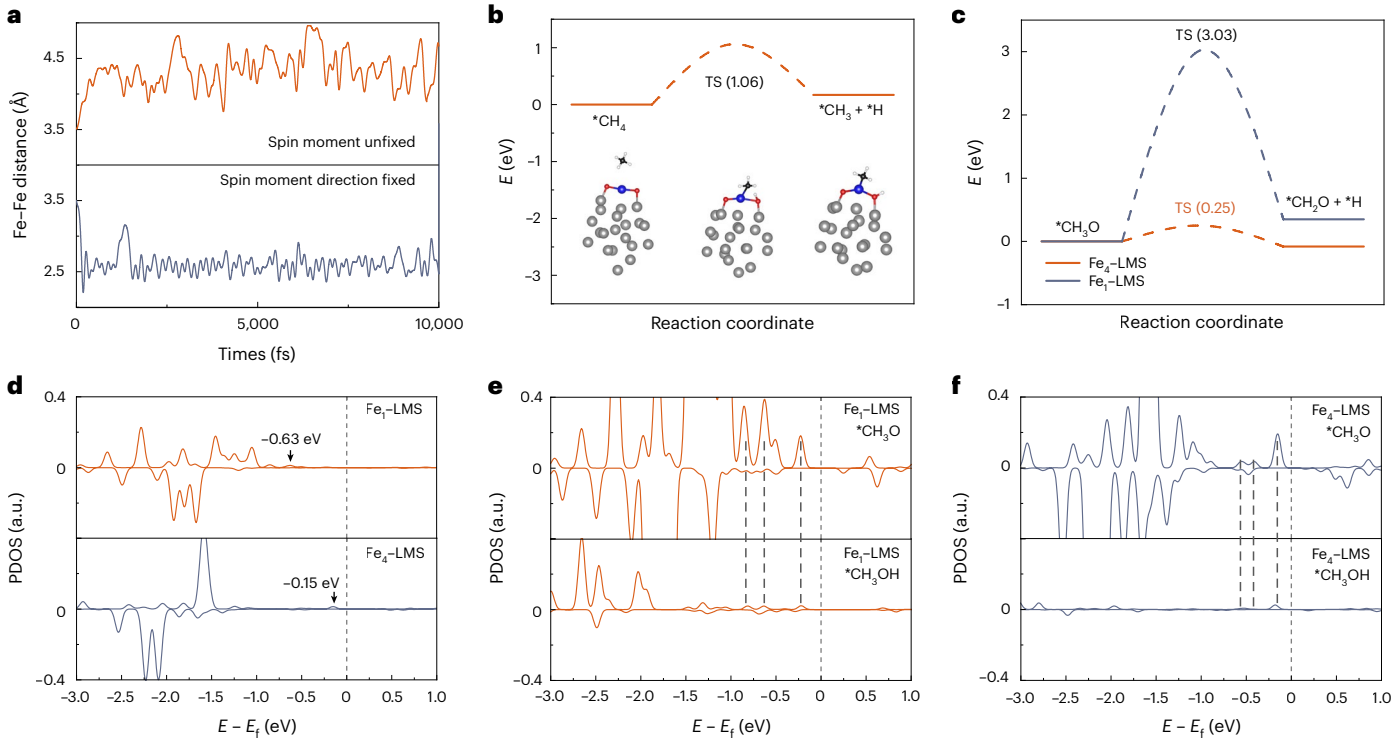

Fig. 5 | Theoretical calculations. a, AIMD simulation trajectories of the Fe–Fe distance as a function of time. The initial distance between the two iron atoms is 3.5 Å, with the spin moment direction unfixed and fixed, respectively. **b**, Calculated Gibbs free energy profile and schematic diagram of CH_4 to CH_3 on Fe_1–LMS. **c**, Calculated Gibbs free energy profile of partial steps of CH_3O to CH_2O on Fe_1–LMS and Fe_4–LMS. **d**, PDOS of the C of CH_3O in Fe_1–LMS and Fe_4–LMS. **e**, PDOS of the O of CH_3OH and CH_3O in Fe_1–LMS (dashed line indicates the peak position). **f**, PDOS of the O of for CH_3OH and CH_3O in Fe_4–LMS (dashed line indicates the peak position).

(Fig. 4b)[25]. However, no signal of signal was detected on the Fe–LMS immersed in 30% H_2O_2 solution for 1 h (Fig. 4c). Gallium element signals revealed that, with the introduction of oxidants, a portion of the initially zero-valent gallium undergoes oxidation to form Ga_2O_3 (1,117.0 eV to 1,118.2 eV, Supplementary Fig. 30)[26]. These results indicate that iron atoms migrating to the surface are anchored by oxygen atoms, forming Fe–O–Ga structures, which are identified as the active sites. When the catalyst surface is completely oxidized by Ga_2O_3, iron atoms are encapsulated inside and lose the ability to contact with the reactants. Intermediate species of CH_x (285.6 eV) and $*OCH_3$ (286.4 eV) are simultaneously detected on the dispersed catalyst (Fig. 4d)[27,28]. This is probably due to the C–H bond cleavage of CH_4 to generate CH_x, followed by being adsorbed on metal atoms or bonding with oxyen atoms to form $*OCH_3$. $*CO_x$ (289.8 eV) is found as the main intermediate species on the aggregated catalyst (lower spectra in Fig. 4d). A new peak appearing at 293 eV is attributable to the physical adsorption of CO. The gaseous CO is probably generated by the further desorption of $*CO_x$, which has been identified as the main gas product in Fig. 3c.

In situ XAFS (Supplementary Fig. 29c) revealed dynamic changes in the local environment of iron atoms during the reaction. Fe_1–LMS in the absence of a magnetic field showed a 1.5-Å Fe–O peak upon H_2O_2 exposure, signifying formation of the Fe–O bond. With the simultaneous introduction of H_2O_2 and CH_4, this peak shifted +0.1 Å (1.9 → 2.0 Å, Fig. 4f and Supplementary Table 2), indicating Fe–O bond elongation, consistent with in situ XPS data showing bond weakening due to $*OCH_3$ formation. Under a 500-G field, the spectrum of Fe–LMS provided with H_2O_2 lacks a legible peak with respect to the Fe–C/O bond (Fig. 4g,h); however, an enhanced peak at 1.6 Å emerges in the spectrum of Fe–LMS provided with H_2O_2 and CH_4, illustrating the existence of an Fe–C/O bond. Considering that the intermediate species $*CO_x$ was detected in the in situ XPS results for Fe–LMS under similar conditions, it is rational to speculate that the enhanced peak concerning the Fe–C/O bond derives from the formation of intermediate species $*CO_x$ on iron atoms during the reaction period. Here, CO as the main gas product for the CH_3COOH path was additionally introduced into the reaction system at gradually increasing partial pressures (0, 1 and 5 bar). Figure 4i shows ever-heightening peaks of Fe–C/O bonds with gradually increasing CO partial pressures, clarifying that the enhancement of these peaks is associated with the adsorption of *CO. The above results explicitly revealed an apparent distinction of coordination environments for iron atoms under magnetic field switching. The mechanism of the reversible reaction pathway is depicted in Fig. 4g. The magnetic field switching induces reversible conversion of the states of iron atoms between dispersion and agglomeration, resulting in the formation of different intermediate species and thus finally realizing the alteration of the main liquid products.

Theoretical works

To understand the selectivity of reaction pathways due to the structural change of catalysts, we performed ab initio molecular dynamics (AIMD) simulations and density functional theory (DFT) calculations. In the absence of a magnetic field, it is found that two iron atoms in the liquid gallium alloy are inclined to disperse into two iron single atoms due to the entropy effect (Fig. 5a and Supplementary Fig. 31). However, under a magnetic field, the two iron atoms are agglomerated into an iron dimer (Fig. 5a and Supplementary Fig. 32); single iron atoms tend to align their spins uniformly and move along the direction of the field, leading to agglomeration under a magnetic field. In addition, it is found that an iron atom surrounded by gallium metal in the droplet configuration can be pulled out and anchored by the oxygen atoms on the surface (Supplementary Fig. 33). This result is consistent with that obtained from previous in situ experiments, and is based on a comprehensive analysis combining XAFS results (Supplementary Table 2) and AIMD stability assessments (Supplementary Figs. 34 and 35). The structure

of the two O-coordinated iron single atoms is relatively stable without a magnetic field. For the agglomerated iron clusters with an external magnetic field, we chose the tetrahedral Fe_4 with the coordination number of Fe–Fe being 3 for calculations.

Next, we investigated the generation of the Ga–O–Fe structure from H_2O_2 decomposition. We found that H_2O_2 can be easily decomposed into two OH or into O and H_2O on the iron active site without oxygen anchoring (Supplementary Fig. 36a), and this process is barrierless. Once the iron active site is fixed by the released O, H_2O_2 can be formed through the interaction of a hydrogen bond with an adjacent O (Supplementary Fig. 36b,c), and can then dissociate to OOH and H via O–H rupture with a barrier of 0.33 eV (TS1). The O–O bond-cleavage barrier is 0.27 eV through the transition state TS2. Finally, the Ga–O–Fe structure eventually forms on the catalyst surface.

We further researched the process of CH_4 oxidation on Fe_1–LMS and Fe_4–LMS. Figure 5b shows the calculated Gibbs free energy profile of partial steps of CH_4 oxidation to CH_3OH on Fe_1–LMS (see Supplementary Figs. 37–39 for complete steps). CH_4 is initially located on Fe_1–LMS through the iron atom. CH_4 dehydrogenation occurs via TS3 with an energy barrier of 1.05 eV. Then, the generated OOH combines with a CH_3 radical to form CH_3OOH through TS4 (0.44 eV). Apparently, methyl hydroperoxide (CH_3OOH) is the sole first product of peroxide-assisted CH_4 oxidation, which is consistent with a previous study[29]. The CH_3OOH is decomposed into CH_3O and OH via TS5 (0.18 eV) by cleavage of the O–O bond. Finally, CH_3O is readily reduced to methanol (TS6, 0.32 eV). Clearly, the CH_4 dehydrogenation is the rate-determining step with a barrier of 1.05 eV. In addition, the formed CH_3O continues the dehydrogenation with a large barrier of 3.03 eV via TS7 on Fe_1–LMS, which is unfavourable to forming oxides with higher oxidation state (CO, CH_3COOH, etc.) (Fig. 5c and Supplementary Fig. 40).

When the iron single atoms directionally move to form the iron cluster catalyst (Fe_4–LMS) induced by the magnetic field, the CH_4 oxidation pathway is completely altered and the main product is changed into CH_3COOH. Figure 5b shows the calculated Gibbs free energy profile of partial steps of CH_4 oxidation to CH_3COOH on Fe_4–LMS (see Supplementary Figs. 37, 41 and 42 for complete steps). CH_4 dehydrogenation produces CH_3 via TS8 with a barrier of 0.67 eV. Then, the formed CH_3 combines with OOH to generate CH_3O and OH (exothermic by 4.11 eV). The CH_3O is changed into CO via three continuous dehydrogenation steps with barriers of 0.25, 0.62 and 0.79 eV through TS9–TS11, respectively. By comparison, this reaction is more difficult to achieve on Fe_1–LMS with a high barrier of 3.03 eV (Fig. 5c and Supplementary Fig. 40). The CO couples with CH_3 to generate CH_3CO via TS12 (0.47 eV). CH_3CO continues to combine with OH to produce CH_3COOH through TS13 (0.95 eV). In terms of kinetics, the reaction $CH_3CO + OH \rightarrow CH_3COOH$ is the rate-determining step with a barrier of 0.95 eV. Furthermore, the formation of CH_3OH ($CH_3O + H \rightarrow CH_3OH$) on Fe_4–LMS is difficult due to the high barrier of 1.47 eV via TS14 (Supplementary Fig. 42)

We further probed the intrinsic reasons for the selectivity of CH_4 oxidation on Fe_1–LMS and Fe_4–LMS. We determined that the intermediate CH_3O is the crossover point between the CH_3OH and CH_3COOH pathways. The projected density of states (PDOS) of C–H bonding of CH_3O in Fe_1–LMS and Fe_4–LMS (Fig. 5d) indicate that the DOS peak (−0.15 eV) of carbon is closer to the Fermi level in Fe_4–LMS than in Fe_1–LMS (−0.63 eV), which makes it more likely to lose electrons and become oxidized. Therefore, the CH_3O easily undergoes dehydrogenation (oxidation) in Fe_4–LMS. We also calculated the orbitals and PDOS of the O–H bonding of CH_3OH and the O of CH_3O in Fe_1–LMS and Fe_4–LMS (Fig. 5e,f). We found that the DOS peak position of the O of CH_3OH is more similar to that of the O of CH_3O near the Fermi level in Fe_1–LMS (Fig. 5e) compared with in Fe_4–LMS (Fig. 5f). Therefore, the CH_3O easily undergoes hydrogenation in Fe_1–LMS. In addition, the *d*-orbital centre (−2.00 eV) of iron in Fe_4–LMS is closer to the Fermi level than that in Fe_1–LMS (−2.25 eV), and thus exhibits a stronger adsorption energy for CH_3O (−2.94 eV) than that of Fe_1–LMS (−2.47 eV) (Supplementary Fig. 44a). Therefore, CH_3O is suitable for continuous dehydrogenation reactions to generate CO in Fe_4–LMS, and CH_3O is suitable for hydrogenation and desorption (desorption energy, 0.55 eV) in Fe_1–LMS. We also found that O-2*p* and Fe-3*d* form antibonding σ_1^*, π_1^* and π_2^* bonds between CH_3O with Fe_1–LMS (Supplementary Fig. 44a,c) and form an antibonding σ_1^* bond between CH_3O with Fe_4–LMS (Supplementary Fig. 44a,f) through crystal orbital Hamiltonian population calculations of iron and oxygen (Supplementary Fig. 44b,e).

In addition, CO is the key intermediate for producing C2 products through C–C coupling. In Fe_4–LMS, the barrier of C–C coupling on Fe–Fe active sites is 0.47 eV through TS12 (Supplementary Figs. 41 and 42). In Fe_1–LMS, the barrier of C–C coupling on Fe–Ga active sites is as high as 0.94 eV via TS15 (Supplementary Fig. 45). In addition, CO only forms with difficulty due to the high barrier of 3.03 eV for CH_3O dehydrogenation (Supplementary Fig. 40). Therefore, the C–C coupling for the C2 product (CH_3COOH) requires the iron cluster to simultaneously anchor the CO and CH_3, which is attributed to the enhanced CO adsorption energy on the iron cluster (1.71 versus 0.70 eV).

Conclusions

We have prepared a catalyst of Fe–LMS with a sensitive magnetic field response, which enables reversible conversion of the main liquid products of CH_4 oxidation (that is, CH_3OOH and CH_3COOH) under the external control of a magnetic field at room temperature. We attain high production rates and selectivities and steady reproducibility. The external magnetic field manipulates the spin orientation of the iron single atoms, guiding the directional movement and agglomeration of the iron atoms from a dispersion state. Our work may provide a guide for the precise control of reaction pathway of a catalyst via a magnetic field, showcasing potential benefits of magnetic-based catalysis adjustment in improving reaction selectivity, streamlining reaction apparatus and conditions, and reducing both energy consumption and operational costs for industrial synthesis.

Online content

Any methods, additional references, Nature Portfolio reporting summaries, source data, extended data, supplementary information, acknowledgements, peer review information; details of author contributions and competing interests; and statements of data and code availability are available at https://doi.org/10.1038/s41565-025-02029-5.

References

1. Gunsalus, N. J. et al. Homogeneous functionalization of methane. *Chem. Rev.* **117**, 8521–8573 (2017).
2. Labinger, J. A. & Bercaw, J. E. Understanding and exploiting C–H bond activation. *Nature* **417**, 507–514 (2002).
3. Schwach, P., Pan, X. & Bao, X. Direct conversion of methane to value-added chemicals over heterogeneous catalysts: challenges and prospects. *Chem. Rev.* **117**, 8497–8520 (2017).
4. Hickman, D. & Schmidt, L. Production of syngas by direct catalytic oxidation of methane. *Science* **259**, 343–346 (1993).
5. Qi, J. et al. Selective methanol carbonylation to acetic acid on heterogeneous atomically dispersed ReO_4/SiO_2 catalysts. *J. Am. Chem. Soc.* **142**, 14178–14189 (2020).
6. Daeneke, T. et al. Liquid metals: fundamentals and applications in chemistry. *Chem. Soc. Rev.* **47**, 4073–4111 (2018).
7. Markvicka, E. J., Bartlett, M. D., Huang, X. & Majidi, C. An autonomously electrically self-healing liquid metal–elastomer composite for robust soft-matter robotics and electronics. *Nat. Mater.* **17**, 618–624 (2018).
8. Tang, J. et al. Dynamic configurations of metallic atoms in the liquid state for selective propylene synthesis. *Nat. Nanotechnol.* **19**, 306–310 (2024).

9. Garcés-Pineda, F. A., Blasco-Ahicart, M., Nieto-Castro, D., López, N. & Galán-Mascarós, J. R. Direct magnetic enhancement of electrocatalytic water oxidation in alkaline media. *Nat. Energy* **4**, 519–525 (2019).
10. Ren, X. et al. Spin-polarized oxygen evolution reaction under magnetic field. *Nat. Commun.* **12**, 2608 (2021).
11. Zhou, G. et al. Spin-state reconfiguration induced by alternating magnetic field for efficient oxygen evolution reaction. *Nat. Commun.* **12**, 4827 (2021).
12. Wertheim, G. K. *Mössbauer Effect: Principles and Applications* (Academic Press, 2013).
13. May, L. *An Introduction to Mössbauer Spectroscopy* (Springer, 2012).
14. Cotton, E. *The Mossbauer Effect and its Applications* (Centre d'Etudes Nucleaires, 1960).
15. Long, G. J. & Grandjean, F. *Mössbauer Spectroscopy Applied to Inorganic Chemistry* Vol. 3 (Springer, 2013).
16. Lund, A., Shiotani, M. & Shimada, S. *Principles and Applications of ESR Spectroscopy* (Springer, 2011).
17. Charles Jr, P. & Farach, H. A. *Handbook of Electron Spin Resonance* Vol. 2 (Springer, 1999).
18. Shukla, A. K. *ESR Spectroscopy for Life Science Applications* (Springer, 2021).
19. Hoshyargar, F., Crawford, J. & O'Mullane, A. P. Galvanic replacement of the liquid metal galinstan. *J. Am. Chem. Soc.* **139**, 1464–1471 (2017).
20. Liu, T., Sen, P. & Kim, C.-J. Characterization of nontoxic liquid-metal alloy galinstan for applications in microdevices. *J. Microelectromech. Syst.* **21**, 443–450 (2011).
21. Zhang, X.-D. et al. Experimental investigation of galinstan based minichannel cooling for high heat flux and large heat power thermal management. *Energy Convers. Manag.* **185**, 248–258 (2019).
22. Shan, J., Li, M., Allard, L. F., Lee, S. & Flytzani-Stephanopoulos, M. Mild oxidation of methane to methanol or acetic acid on supported isolated rhodium catalysts. *Nature* **551**, 605–608 (2017).
23. Tang, Y. et al. Single rhodium atoms anchored in micropores for efficient transformation of methane under mild conditions. *Nat. Commun.* **9**, 1–11 (2018).
24. Birnie, D. P. & Bendzko, N. J. ^{1}H and ^{13}C NMR observation of the reaction of acetic acid with titanium isopropoxide. *Mater. Chem. Phys.* **59**, 26–35 (1999).
25. Biesinger, M. C. et al. Resolving surface chemical states in XPS analysis of first row transition metals, oxides and hydroxides: Cr, Mn, Fe, Co and Ni. *Appl. Surf. Sci.* **257**, 2717–2730 (2011).
26. Schön, G. Auger and direct electron spectra in X-ray photoelectron studies of zinc, zinc oxide, gallium and gallium oxide. *J. Electron. Spectrosc. Relat. Phenom.* **2**, 75–86 (1973).
27. Liu, Z. et al. Water-promoted interfacial pathways in methane oxidation to methanol on a CeO_2–Cu_2O catalyst. *Science* **368**, 513–517 (2020).
28. Lustemberg, P. G. et al. Direct conversion of methane to methanol on Ni-ceria surfaces: metal–support interactions and water-enabled catalytic conversion by site blocking. *J. Am. Chem. Soc.* **140**, 7681–7687 (2018).
29. Yu, T. et al. Highly selective oxidation of methane into methanol over Cu-promoted monomeric Fe/ZSM-5. *ACS Catal.* **11**, 6684–6691 (2021).

Methods

Synthesis methods

Preparation of Fe–LMS, Fe@Ga–In, Fe@Ga–Sn and Fe@Ga. The synthesis Fe–LMS must be performed in a nitrogen atmosphere throughout to prevent oxygen oxidation.

Gallium (99.999%) was first melted at 50 °C in a beaker. Subsequently, 7 g molten gallium metal was mixed with 2 g indium powder (99.999%) and 1 g tin powder (99.999%), followed by vigorous stirring at 160 °C for 5 h. Different amounts of iron powder (0.1–2 g, 99.999%) were added into the liquid metal alloy followed by manual stirring until the iron powder was entirely dissolved. Then, 100 µl of 5% hydrochloric acid was added to keep the alloy in a liquid state. The obtained liquid metal catalyst Fe–LMS was stored in an oxygen-free container.

After adjusting the feeding ratio to Fe:Ga:In to 0.1:7:3 (w/w/w/), the aforementioned process was repeated to obtain Fe@Ga–In. After adjusting the feeding ratio to Fe:Ga:Sn to 0.09:7:1 (w/w/w/), the aforementioned process was repeated to obtain Fe@Ga–Sn. After adjusting the feeding ratio to Fe:Ga to 0.1:10 (w/w) and adjusting the temperature to 200 °C, the aforementioned process was repeated to obtain Fe@Ga.

Preparation of Fe–LMS@H_2O. First, 10 mg of prepared Fe–LMS was added to 20 ml of deionized water, and the mixture was then placed in a room-temperature water bath and agitated ultrasonically for 30 min until the solution became turbid. The synthesis of Fe–LMS@H_2O does not require a protective atmosphere. Fe–LMS@H_2O is a suspension, and the prepared Fe–LMS@H_2O must be used immediately to avoid sedimentation.

Catalytic performance evaluation

Methane oxidation by Fe–LMS with no magnetic field. Oxidation of CH_4 was performed in a stainless-steel Teflon-lined autoclave with a volume of 100 ml. Typically, 10 mg catalyst Fe–LMS, 20 ml deionized water and 5 ml H_2O_2 (30%) were added to the autoclave. Hydrochloric acid was added dropwise until the pH of the solution approached 4. The autoclave was flushed three times with methane and then pressurized with methane to the desired pressures (0.5–3.0 MPa CH_4, 99.999%). The reaction proceeded for 1 h at room temperature. The autoclave with obtained products was cooled in ice water for 20 min prior to analysis. Liquid products were quantified by ^{1}H and ^{13}C NMR spectroscopy. The gas-phase products are discharged through the reactor's exhaust valve and collected in a gas bag, which is subsequently transferred to the GC for analysis.

Methane oxidation by Fe–LMS with a magnetic field. The CH_4 oxidation reaction was carried out in a closed high-pressure autoclave. The high-pressure reactor was placed between two parallel permanent magnets, and the intensity of the magnetic field was controlled by an external distance-adjustment device. About 10 mg catalyst, 20 ml deionized water and 5 ml H_2O_2 (30%) were added to the autoclave. Hydrochloric acid was added dropwise until the solution pH approached 4. The autoclave was flushed three times and then pressurized with methane to the desired pressure (0.5–3.0 MPa CH_4, 99.999%). The reaction mixture was left at room temperature for 1 h. The magnetic field can be regulated over the range 0–1,200 G. The autoclave with obtained products was cooled in ice water for 20 min prior to analysis. Liquid products were quantified by ^{1}H and ^{13}C NMR spectroscopy. The gas-phase products are discharged through the reactor's exhaust valve and collected in a gas bag, which is subsequently transferred to the GC for analysis.

Methane oxidation by Fe–LMS@H_2O with magnetic field switching. The CH_4 oxidation reaction was carried out in a closed high-pressure autoclave. The high-pressure reactor was placed between two parallel permanent magnets, and the intensity of the magnetic field was controlled by an external distance-adjustment device. First, 2 ml Fe–LMS@H_2O solution, 20 ml deionized water and 5 ml H_2O_2 (30%) were added to the autoclave. Hydrochloric acid was added dropwise until the solution pH approached 4. The autoclave was flushed three times and then pressurized with methane to the desired pressure (2.0 MPa CH_4, 99.999%). The reaction mixture was left at room temperature for 1 h. Tests were conducted under magnetic fields of 0, 50, 100, 150, 175, 200, 210, 250, 300, 400 and 500 G. The autoclave with obtained products was cooled in ice water for 20 min prior to analysis. Liquid products were quantified by ^{1}H and ^{13}C NMR spectroscopy. The gas-phase products are discharged through the reactor's exhaust valve and collected in a gas bag, which is subsequently transferred to the GC for analysis.

Methane oxidation by Fe–LMS with additional CO and applying a magnetic field. The CH_4 oxidation reaction was carried out in a closed high-pressure autoclave. The high-pressure reactor was placed between two parallel permanent magnets, and the intensity of the magnetic field was controlled by an external distance-adjustment device. About 100 µl catalyst, 19 ml deionized water and 1 ml H_2O_2 (30%) were added to the autoclave. Hydrochloric acid was added dropwise until the pH of the solution approached 4. The autoclave was flushed three times and then pressurized with CO to the desired pressure (0.1–1.0 MPa), and 2 MPa CH_4 was then added into the reaction system. The reaction proceeded for 1 h at room temperature, under 0 or 500 G. The obtained products were cooled in ice water for 10 min prior to analysis. Liquid products were quantified by ^{1}H and ^{13}C NMR spectroscopy. Gas products were quantified by GC.

Reproducibility of liquid product conversion. First, 100 µl fresh catalyst, 20 ml deionized water and 5 ml H_2O_2 (30%) were added to the autoclave, which was flushed three times with deionized water and then pressurized with 2.0 MPa methane. Hydrochloric acid was added dropwise until the pH of the solution approached 4. The reaction was performed while switching the magnetic field on–off 11 times at 1-h intervals. The catalyst was washed with hydrochloric acid (pH 4) after each 1-h reaction to remove the oxidation film on the catalyst. The reactants and washed catalyst were then placed back into the autoclave for the next reaction. The obtained products were cooled in ice water for 10 min prior to analysis. Liquid products were quantified by ^{1}H and ^{13}C NMR spectroscopy.

Characterization methods

X-ray diffraction measurements were recorded on a Rigaku Miniflex-600 diffractometer using Cu Kα radiation (λ = 0.15406 nm) with a step size of 0.02° and a counting time of 0.5 s. Transmission electron microscopy images were recorded on a Hitachi H-7700 operated at 100 kV. Scanning electron microscopy images were recorded on a Supra 40. A Quantum Design MPMS3 was used for magnetic moment testing. Elemental analysis was performed by inductively coupled plasma atomic emission spectrometry using an Optima 7300 DV spectrometer. Liquid products were quantified by NMR spectroscopy. Measurements were conducted on a Bruker Avance-III 400 spectrometer. ^{1}H NMR spectra were recorded with a 2-s recycle delay, for 64 scans, using dimethyl sulfoxide as an internal standard. ^{13}C NMR spectra were recorded with a 10-s recycle delay, for 2,048 scans. Gaseous products were quantified by a GC equipped with a 5-Å molecular sieve, a Porapak Q 80/100 mesh, and SE-30 and HP-Al_2O_3/S columns using helium (ultrahigh purity) as carrier gas.

In situ electron microscopy and corresponding atomic-level EDS mapping

Aberration-corrected HAADF-STEM images and corresponding EDS maps were recorded on a FEI-Titan Cubed Themis G2 300 STEM. Frozen sample rods were used to load samples, allowing for cooling with liquid nitrogen during testing. Before electron microscopy imaging, the samples were subjected to magnetic fields of 0 G and 500 G and frozen with liquid nitrogen for 10 min to fix the structure.

In situ X-ray 3D CT

In situ X-ray 3D CT was carried out at beamline BL07W of the National Synchrotron Radiation Laboratory. The sample holder, containing the nickel grid, was transferred to the chamber of a transmission soft X-ray microscope, where an elliptical capillary condenser focused the soft X-ray beam onto the cells for observation. In the sample chamber, the magnetic field is adjusted by controlling the distance between the natural magnet and the sample holder. For the generation of 3D volumes, the cells were rotated from −60° to +60°, capturing a continuous series of 121 projected images at 1° intervals with a 2-s exposure time. X-ray energies is 706 eV and 715 eV (covering the Fe L3 edge) were used. Alignment of the tilt series was performed using XMController, and 3D CT reconstruction was carried out using XMReconstruction.

In situ Mössbauer spectroscopy

Mössbauer spectroscopy measurements were conducted using a Wissel MR-2500 spectrometer. For the Fe–LMS sample under a 500-G magnetic field, the field strength at the sample location was adjusted by placing a natural magnet outside the measurement chamber. Each sample weighed 100 mg, and measurements were performed at room temperature in a vacuum environment. The spectral range was set to ±12 mm s^{-1}, with a measurement duration of 24 h.

ESR

ESR was performed at the Steady High Magnetic Field Facilities, High Magnetic Field Laboratory, using the following parameters: temperature, 173 K; power, 0.01 mW; central field, 7,000 G; sweep width, 14,000 G; modulation frequency, 100 kHz; modulation amplitude, 2.00 G. The samples were frozen at 173 K for 10 min under magnetic fields of 0 G and 500 G, respectively, and the iron powder standard samples were frozen at 0 G and 173 K for 10 min before testing.

NAP-XPS measurements

NAP-XPS measurements were performed using a system located at Shanghai Tech University. This system was manufactured by SPECS Surface Nano Analysis (Supplementary Fig. 28). The facility consists of a main chamber, a preparation chamber and a load–lock chamber. The analysis chamber is equipped with a PHOIBOS NAP hemispherical electron energy analyser, a microfocus monochromatized Al Kα X-ray source with a beam diameter of 300 µm, a SPECS IQE-11A ion gun and an infrared laser heater. Fe_1–LMS (1.1 wt%) was dropped onto a clean silicon wafer and dried at room temperature. Having installed the sample in the analysis chamber, high-purity CH_4 was fed into the chamber up to a pressure of 0.4 mbar. After collecting the C 1*s* spectra, a flask containing 30% H_2O_2 solution was connected to the XPS testing chamber (see Supplementary Fig. 29 for photographs). The negative pressure within the chamber ensured the controlled evaporation of H_2O_2 into the atmosphere, and a new series of C 1*s* spectra were acquired. The above results were recorded as the dispersed state. We then replaced the iron content to give a concentration of 9.8 wt%, repeated the above experiment, and recorded the results as the aggregated state.

It should be noted that due to the stringent pressure requirements of NAP-XPS, the testing conditions represent a compromise compared with those of the actual catalytic experiments. Below, we provide a detailed justification for these compromises:

(1) The primary objective of NAP-XPS is to capture reaction intermediates. Given the technique's qualitative nature and operational constraints, direct introduction of a liquid-phase environment was unfeasible. Instead, we used a 0.13-mbar H_2O_2 (30% solution) vapour atmosphere to approximate the H_2O_2 liquid environment present in the actual catalytic reaction. Although this substitution differs from the exact reaction conditions, it enables the identification of key intermediates under operando conditions.

(2) As discussed elsewhere (Supplementary Figs. 20–24), HCl serves to prevent complete oxidation of the catalyst surface in the catalytic reaction. However, during the NAP-XPS measurement timeframe, the oxidative capacity of the H_2O_2 atmosphere is insufficient to fully oxidize the catalyst surface; thus, its absence does not alter the observed reaction pathway. Furthermore, due to the pressure limitations of NAP-XPS, the concentrations of the primary reactants (CH_4 and H_2O_2) were already lower than those in the catalytic process. Introducing HCl would further reduce reactant concentrations, adversely affecting the signal-to-noise ratio and the reliability of the measurements. Consequently, HCl was deliberately excluded from the NAP-XPS experiments to preserve data quality.

In situ XAFS measurements

Fe K-edge (7,112 eV) XAFS spectra were recorded at the 1W1B beamline of the Beijing Synchrotron Radiation Facility. The storage ring was operated at 2.5 GeV, with a maximum electron current of 250 mA. The hard X-ray beam was monochromatized with a Si(111) double-crystal monochromator. For the removal of higher-order harmonics, the X-ray was detuned by 30% for the Fe K-edge. The detection system consists of a 19-element germanium solid-state detector and a Lytle detector. In situ XAFS measurements were performed using a home-made reactor (10 ml) with a vitreous carbon window (diameter, 6 mm; Supplementary Fig. 30). A catalyst-coated carbon-fibre paper (diameter, ~5 mm) was sealed behind the window. Spectra were collected in fluorescence mode. The spectrum of a iron metal foil was collected concomitantly for internal energy calibration. Three spectra were averaged for each dataset. The catalysts used in the measurements are Fe–LMS–1% and Fe–LMS–10%, with precise iron loadings of 1.1 wt% and 9.8 wt%, respectively. To investigate the influence of the self-absorption effect, test samples were collected at incidence angles of 45° and 15°, respectively.

XAFS data analysis

Extended X-ray absorption fine structure (EXAFS) data were processed and analysed following standard procedures within the ATHENA module implemented in the IFEFFIT library software package. The Fe K-edge k^3-weighted $\chi(k)$ data in the *k*-space were Fourier-transformed to the real space (*R*) with Hanning windows (dk = 1.0 $Å^{-1}$) to separate out EXAFS contributions from different coordination shells. Effective backscattering amplitudes and phase shifts were calculated using the ab initio code FEFF8.054. For the FeGa sample, a *k*-rage of 2.5–12.1 $Å^{-1}$ (Δk) was used and the curve fittings in the *R* space were carried out within the range 1.0–3.0 Å (ΔR). The number of independent points was: $N_{ipt} = 2\Delta k \times \Delta R/\pi = 2 \times (12.1 - 2.5) \times (3.0 - 1.0)/\pi \approx 12$. The fitting ranges of all the other samples are listed below Supplementary Table 2, and the numbers of their independent points were calculated similarly; all the samples had more than nine independent points.

The Fourier-transformed curves for Fe–LMS, Fe–LMS–B, Fe–LMS–H_2O_2–B and Fe–LMS–H_2O_2–CH_4–B showed a wide peak at 2.30 Å, which can be assigned to the combination of two kinds of Fe–Ga coordination with different structures, and a two-shell structure model with two different kinds of Fe–Ga scattering paths was used for fitting. For Fe–LMS–H_2O_2 and Fe–LMS–H_2O_2–CH_4, besides the wide peak at 2.30 Å from the Fe–Ga coordination, two distinct peaks at 1.50 Å and 1.58 Å arise due to Fe–O and Fe–C bonds. Consequently, a three-shell structure model with one Fe–O/C path and two different Fe–Ga scattering paths was used to fit the data of both samples.

During curve fittings, the amplitude reduction factor S_0^2 was fixed at a value of 0.78 as determined by fitting the data for a iron foil. For the Fe–LMS sample, the coordination numbers, interatomic distances (*R*) and energy shifts (ΔE_0) for both Fe–Ga paths were treated as adjustable parameters, and the energy shifts (ΔE_0) for the two paths were considered to be the same.

Disorder factor (Debye–Waller factor, σ^2). A single σ^2 value is used for one or two Fe–Ga paths within the same sample, set as an adjustable parameter. For Fe–LMS–B samples, the Fe–Fe path is set as an adjustable parameter. To reduce the number of adjustable parameters in subsequent sample fittings, especially for Fe–LMS–H_2O_2 and Fe–LMS–H_2O_2–CH_4, where three paths are utilized, the σ^2 value for the Fe–Fe path is set to be the same as that of Fe–LMS–B. The Fe–C/O paths in the remaining samples are set as adjustable parameters.

The actual number of adjustable parameters, $N_{para} = 5$, was lower than the maximum number $N_{ipt} = 12$. All of the other samples were treated similarly, and their actual numbers of adjustable parameters were all lower than their independent points. The structural parameters obtained from fitting are listed in Supplementary Table 1. The R factor obtained for every fit is not larger than 0.031, indicating a good quality of the fitting.

Self-absorption correction. Based on iron mass fractions of 1% and 10% in the GaInSn alloy, self-absorption correction was applied using the self-absorption correction function in Athena. The incident and exit angles were set at 45°, reflecting the actual testing conditions, and the fluo-$\mu(E)$ algorithm and troger-$\chi(k)$ algorithm were used for XANES and EXAFS corrections, respectively.

DFT calculations

A vacuum spacing of 10 Å was applied in three directions for all constructed models to prevent interactions between periodic images. All DFT calculations were performed with the Vienna Ab initio Simulation Package (VASP)[30]. The exchange-correlation interactions were treated using the Perdew–Burke–Ernzerhof functional[31] within the generalized gradient approximation. The projector augmented wave[32] was used to treat the inert core electrons. Spin polarization was implemented in all calculations. To simulate the presence of an external magnetic field, noncollinear magnetic calculations were carried out, with the direction of spin moment fixed along the positive x axis, while allowing the magnitude of the magnetic moments to relax. A plane-wave kinetic energy cut-off of 400 eV was used throughout all calculations. The Brillouin zone was sampled with a 1 × 1 × 1 Monkhorst–Pack k-point mesh. The strongly localized 3d orbitals of iron were treated by the DFT + U method with an effective U value of 3 eV (refs. 33,34). The electronic energy convergence criteria were set to 10^{-5} eV, and the force convergence threshold was 0.02 eV Å^{-1}. The climbing-image nudged elastic band method[35] was used to identify transition state structures. All optimized structures were confirmed as ground states (zero imaginary frequency) or transition states (one imaginary frequency) by performing vibrational frequency analysis. Long-range dispersion interactions were included using Grimme's DFT-D3 method[36]. Solvent effects were considered by applying an implicit solvation model for water via the VASPsol module[37,38]. Bader charge analysis was performed to quantify electron transfer. PDOS calculations and orbital interaction analyses were conducted using the VASPKIT toolkit[39].

AIMD simulations

The structural changes and dynamic properties of the Fe_n–LMS were investigated with AIMD simulations using VASP. The same computational settings were used as in the static DFT calculations, including convergence criteria, plane-wave kinetic energy cut-off, k-point mesh, exchange-correlation functional, spin treatment, DFT-D3 dispersion correction, and the DFT + U correction. Canonical NVT ensemble and Nosé–Hoover thermostats[40] were adopted at 298.15 K with a time step of 1 fs.

Data availability

The data that support the findings of this study are available within the Article and its Supplementary Information. Other relevant data are available from the corresponding authors upon reasonable request. Source data are provided with this paper.

References

30. Kresse, G. & Furthmüller, J. Efficient iterative schemes for ab initio total-energy calculations using a plane-wave basis set. *Phys. Rev. B* **54**, 11169–11186 (1996).
31. Perdew, J. P., Burke, K. & Ernzerhof, M. Generalized gradient approximation made simple. *Phys. Rev. Lett.* **77**, 3865 (1996).
32. Kresse, G. & Joubert, D. From ultrasoft pseudopotentials to the projector augmented-wave method. *Phys. Rev. B* **59**, 1758 (1999).
33. Zhou, J. & Sun, Q. Magnetism of phthalocyanine-based organometallic single porous sheet. *J. Am. Chem. Soc.* **133**, 15113–15119 (2011).
34. Mishra, S. et al. Contrasting magnetic and magnetoelectric properties of $LuMWO_6$ (M=Fe and Cr): role of spin frustration and noncollinear magnetic structure. *Phys. Rev. B* **108**, 014435 (2023).
35. Henkelman, G., Uberuaga, B. P. & Jónsson, H. A climbing image nudged elastic band method for finding saddle points and minimum energy paths. *J. Chem. Phys.* **113**, 9901–9904 (2000).
36. Grimme, S., Antony, J., Ehrlich, S. & Krieg, H. A consistent and accurate ab initio parametrization of density functional dispersion correction (DFT-D) for the 94 elements H-Pu. *J. Chem. Phys.* **132**, 154104 (2010).
37. Mathew, K., Sundararaman, R., Letchworth-Weaver, K., Arias, T. & Hennig, R. G. Implicit solvation model for density-functional study of nanocrystal surfaces and reaction pathways. *J. Chem. Phys.* **140**, 84106 (2014).
38. Mathew, K., Kolluru, V., Mula, S., Steinmann, S. N. & Hennig, R. G. Implicit self-consistent electrolyte model in plane-wave density-functional theory. *J. Chem. Phys.* **151**, 234101 (2019).
39. Wang, V., Xu, N., Liu, J.-C., Tang, G. & Geng, W.-T. VASPKIT: a user-friendly interface facilitating high-throughput computing and analysis using VASP code. *Comput. Phys. Commun.* **267**, 108033 (2021).
40. Martyna, G. J., Klein, M. L. & Tuckerman, M. Nosé–Hoover chains: the canonical ensemble via continuous dynamics. *J. Chem. Phys.* **97**, 2635–2643 (1992).

Acknowledgements

This work was supported by the China Ministry of Science and Technology (2021YFA1500404), the National Natural Science Foundation of China (92261105 and 22221003), the Key Program of the National Natural Science Foundation of China (U23A2081), the Anhui Provincial Natural Science Foundation (2108085UD06, 2208085UD04), the Anhui Provincial Key Research and Development Project (2023z04020010, 2022a05020053), the Collaborative Innovation Program of Hefei Science Center, CAS (2021HSC-CIP002) and the Joint Funds from Hefei National Synchrotron Radiation Laboratory (KY2060000180 and KY2060000195). We acknowledge the photoemission end stations BL1W1B in the Beijing Synchrotron Radiation Facility, BL14W1 in the Shanghai Synchrotron Radiation Facility, and BL10B and BL11U in the National Synchrotron Radiation Laboratory for providing assistance in characterization. Part of this research was carried out using the SPECS NAP-XPS instrument, which was supported by the ME2 project under contract number 11227902 from the National Natural Science Foundation of China. A portion of this work was supported by the robotic AI-Scientist platform of Chinese Academy of Science. A portion of this work was supported by the Steady High Magnetic Field Facilities in the High Magnetic Field Laboratory belonging to the Chinese Academy of Sciences. The numerical calculations presented in this work were performed on the supercomputer system in the Supercomputing Center of University of Science and Technology of China.

Author contributions

L.Z. and Y.W. conceived and designed the experiments. H. Zhang, Y.Z., S.W., R.H., Z.Z., L.H., Y.M. and H. Zhou performed the synthesis of catalysts and analysed the catalytic performance. F.W. and Z.Z. helped with the spherical aberration electron microscopy tests and discussions. H. Zhang, S.W., X.L., L.H. and T.Y. designed and performed the XAFS experiments. H. Zhang, Y.R., J.C. and Z.L. designed and performed the NAP-XPS experiments. W.Z., Y.W., F.W. and J.J. performed the DFT calculations and analysed the results. H. Zhang, Y.Z., H. Zhou and Y.W. wrote the paper. All of the authors discussed the results and commented on the paper.

Competing interests

The authors declare no competing interests.

Additional information

Supplementary information The online version contains supplementary material available at https://doi.org/10.1038/s41565-025-02029-5.

Correspondence and requests for materials should be addressed to Wenhui Zhong, Lin Hu, Lei Zheng or Yuen Wu.

Peer review information *Nature Nanotechnology* thanks Matteo Cargnello, Jiong Lu and Zhichuan Xu for their contribution to the peer review of this work.